Department of Physics and Astronomy
Heidelberg University

Bachelor Thesis in Physics
submitted by

Larissa Bowien Tolstra

born in Pforzheim (Germany)

2023

Design and characterisation of toroidal cyclotron resonators for the PENTATRAP experiment

This Bachelor Thesis has been carried out by Larissa Bowien Tolstra at the

Max-Planck-Institute of Nuclear Physics in Heidelberg

under the supervision of

Prof. Dr. Klaus Blaum

Abstract

Mass measurements with a relative precision of $\leq 10^{-11}$, like they are performed at the PENTATRAP experiment in Heidelberg, require a high quality detection system to measure the small currents in the order of a few fA, that are induced by the motion of an ion inside a Penning trap. Over the course of this bachelor thesis, toroidal cyclotron resonators are developed and characterised for a future absolute mass measurement of ^{133}Cs at the PENTATRAP experiment. The coils for the resonant circuits in the few ten MHz regime are made from copper wire. Additionally novel designs made from superconducting niob-titanium wire are developed as well. High Q-factors are reached from both approaches. In this context additional tests of voltage controlled resonance frequency tuning with varactor diodes have been successfully performed, reaching tuning ranges of $>10\%$. The impact on Q-factors with different board designs of the cryogenic amplifiers was investigated.

Zusammenfassung

Massenmessungen mit einer relativen Unsicherheit von $\leq 10^{-11}$, wie sie am PENTATRAP-Experiment in Heidelberg durchgeführt werden, erfordern ein hochwertiges Detektionssystem, das auch Ströme im Bereich weniger fA messen kann, welche durch die Bewegung eines in einer Penningfalle gefangenen Ions verursacht werden. Für eine geplante Messreihe der absoluten Masse von ^{133}Cs wurden im Rahmen dieser Bachelorarbeit toroidale Zyklotron-Resonatoren für das PENTA-TRAP-Experiment entwickelt und charakterisiert. Die Spulen für die Resonatoren im Bereich von wenigen zehn MHz werden aus Kupferdraht hergestellt. Zusätzlich werden neuartige Designs aus supraleitendem Niob-Titan-Draht getestet. Beide Ansätze erzielen hohe Q-Faktoren. In diesem Zusammenhang wurden zusätzliche Tests zur spannungsgesteuerten Resonanzfrequenzabstimmung mit Varaktor-Dioden erfolgreich durchgeführt, wobei Abstimmungsbereiche von $>10\%$ erreicht wurden. Die Auswirkungen auf die Q-Faktoren mit verschiedenen Platinen-Designs der kryogenen Verstärker wurden ebenfalls untersucht.

Content

i

List of Figures

List of Tables

1 Motivation

The Standard Model is the most fundamental theory of particle physics classifying the elementary particles and describing three of the four known forces. Although the theory is widely established and was expanded over time, there are still some physical phenomena that cannot be explained like dark matter and dark energy or the observation of neutrino oscillations; constant testing of the standard model is therefore very important.

The Müller Group at the Berkley Physics department performs one of the most precise tests of quantum electrodynamics (QED) and the Standard Model by determining the fine structure constant α, which describes the strength of electromagnetic interactions, and comparing it to the α obtained from the g-2 measurement [1]. To determine α they perform measurements of the recoil energy of ^{133}Cs atoms in a matter-wave interferometer [2]. Using the kinetic energy an atom in the interferometer receives by recoiling from a laser photon, these kind of experiments yield $\frac{\hbar}{m_{Cs}}$. To calculate α from their measurements they use [1]

$$\alpha^2 = \frac{2R_\infty}{c} \frac{m_{Cs}}{m_e} \frac{h}{m_{Cs}} \tag{1}$$

with the Rydberg constant R_∞, the mass of an electron m_e, the speed of light c and the Planck constant h. For this calculation they need to know the mass of ^{133}Cs m_{Cs} with a very high precision. Soon, this will be the limiting factor of their measurements.

When it comes to mass measurements, particle traps, which were first introduced by Paul [3] and Dehmelt [4] in the 20th century, play an important role. In modern atomic and molecular physics. Penning traps are used to isolate and store charged particles in order to perform high precision measurements of basic particle properties like the g-factor (e.g. the ALPHATRAP experiment [5]) or the mass of an ion (e.g. the PENTATRAP experiment [6]). In order to improve the accuracy of the mass of the neutral mass of ^{133}Cs, a mass ratio measurement of ^{133}Cs^{44+} and ^{12}C^{4+} is planned at the PENTATRAP experiment in the foreseeable future. The neutral mass can then be calculated with the mass and the total binding energy $E_{binding}$ of the missing electrons

$$m_{Cs} = m_{Cs^{44+}} + 44 \cdot m_e - E_{binding}. \tag{2}$$

In a Penning trap, the motions of an trapped ion are measured via the detection of so called mirror currents, which are typically in the range of a few fA. Therefore, a sensible and high quality detection system is needed [7], especially for the cyclotron motion of the ions: a cyclotron resonator. A cyclotron resonator, when cooled down to cryogenic temperatures will reduce the radius of the ion motion allowing a more precise determination of the ion's cyclotron frequency.

Over the course of this bachelor thesis work a toroidal cyclotron resonator was developed and adapted for the future $^{133}\text{Cs}^{44+}$ mass measurement at the PENTATRAP experiment. The first part of this thesis gives a brief introduction to the physics of Penning traps. Next, the design and characterisation of the resonant circuit is addressed and measurements of the quality factor were performed. Afterwards, the tuning of the resonance frequency with varactor diodes was examined. In the last part, the signal of the resonator was detected using a cryogenic amplifier.

2 Theory of Penning Trap Physics

The following chapter provides a short summary of the fundamental principles for storing and detecting charged particles in a Penning trap. Section 2.1 describes briefly how a Penning trap works, while section 2.2 explains the motions of a trapped ion. Section 2.3 then goes on to describe the detection of these motions, whereas specifics for the detection and "cooling" of the modified cyclotron motion are further discussed in 2.3.1 and 2.3.2.

2.1 Penning Traps

According to the Earnshaw-Theorem [8], it is not possible to trap a charged particle solely with just an electrostatic or magnetostatic field, which is why a Penning trap uses a combination of both. A strong homogeneous magnetic field in axial direction ensures the radial confinement of the ion's motion, while an electric quadrupole field is responsible for the restriction in axial direction.

In a purely magnetic field $\mathbf{B}$ an ion with charge q, mass m and velocity $\mathbf{v}$ experiences the Lorentz force $\mathbf{F_L}$ given by

$$\mathbf{F_L} = q \cdot \mathbf{v} \times \mathbf{B}, \tag{3}$$

which causes the ion to move in a circular orbit perpendicular to the magnetic field lines with a free cyclotron frequency ν_c of

$$\nu_c = \frac{1}{2\pi} \frac{q}{m} B. \tag{4}$$

The electric quadrupole field can be generated by applying DC voltages onto a set of trap electrodes. In an ideal hyperbolic Penning trap the trap electrodes consist of two end cap electrodes and a ring electrode. However, in most of the presently operated Penning trap experiments, cylindrical electrodes are used instead [9–11], because the manufacturing process is easier and the traps can be easily stacked and operated with more precision. Since the electrode structure of a cylindrical Penning trap is open along the axis of symmetry (see figure 1), the ion can be easily brought in and out of the trap, making the preparation or "loading" of the charged particle much easier. Cylindrical electrodes also provide easier laser access along the axis, e.g. for laser cooling.

The PENTATRAP experiment located at the Max Planck Institute for Nuclear Physics (MPIK) in Heidelberg uses a setup of five Penning traps to perform mass-ratio measurements on highly charged, heavy ions with a relative precision better than 10^{-11} [12, 13]. Each Penning trap contains a stack of five cylindrical ring electrodes (figure 1). The two additional correction electrodes are used to suppress higher order anharmonic terms of the electric field around the trap center [6].
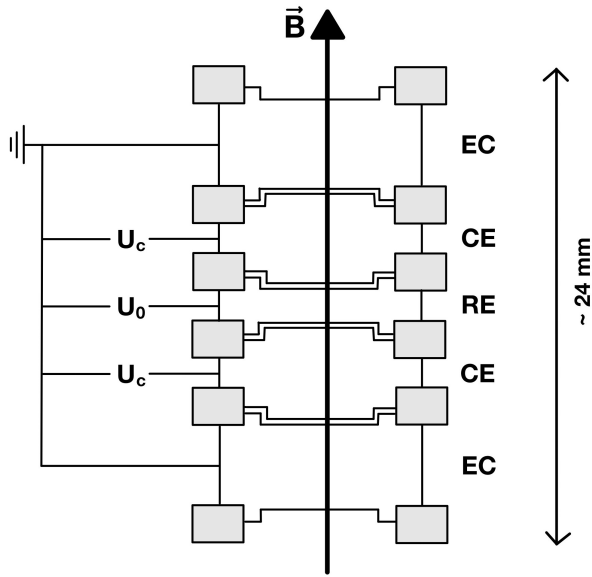
Figure 1: Cross-sectional illustration of a Penning trap consisting of a stack of five cylindrical electrodes. A trap voltage U_0 is applied between both end cap electrodes (EC) and the ring electrode (RE). To correct for anharmonic terms in the electric field a correction voltage U_c is applied to the correction electrodes (CE). The figure is based on Fig. 1 in [14].

2.2 Ion Motion Inside a Penning Trap

The superposition of the magnetic and electric fields as described before in 2.1 is an ideal field configuration. Solving the equations of motion for this case results in three harmonic eigenmotions [15], that are depicted in figure 2.

In axial direction the electric quadrupole field causes the ion to oscillate between
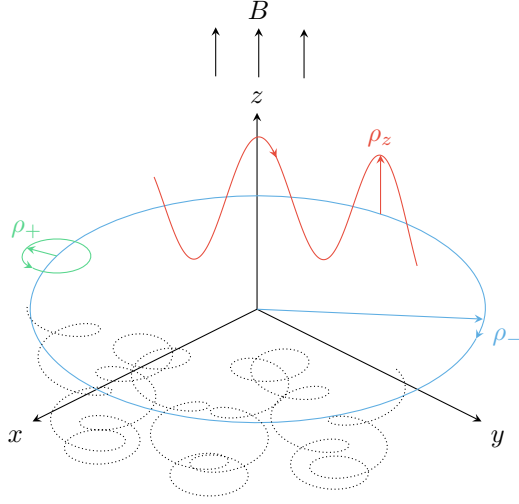
Figure 2: The figure illustrates the motion of an ion inside an ideal Penning trap. The three harmomic eigenmotions are pictured in colour: the axial motion in red, the modified cyclotron motion in green and the magnetron motion in blue. The black dotted line is a superposition of all three and depicts the total trajectory of the trapped ion.

the outer electrodes of the trap with the axial frequency ν_z

$$\nu_z = \frac{1}{2\pi}\sqrt{\frac{q \cdot U_0}{m \cdot d_0^2}}, \tag{5}$$

with d_0 being a characteristic parameter of the trap depending on its geometry. The radial motion consists of the modified cyclotron motion with frequency ν_+ and the magnetron motion with frequency ν_- given by

$$\nu_\pm = \frac{1}{2}(\nu_c \pm \sqrt{\nu_c^2 - 2\nu_z^2}). \tag{6}$$

The magnetron motion is merely an additional drift motion caused by the cross product of the electric and magnetic field $\mathbf{E} \times \mathbf{B}$. For typical ion masses and trap parameters the frequency succession is

$$\nu_c > \nu+ >> \nu_z >> \nu_-. \tag{7}$$

The three eigenfrequencies are directly related to the free cyclotron frequency ν_c via the invariance theorem [15–17]

$$\nu_c^2 = \nu_+^2 + \nu_z^2 + \nu_-^2, \tag{8}$$

which remains valid even if there are minor deviations from the ideal trap geometry or the trap is not perfectly aligned within the magnetic field.

If the magnetic field strength $\mathbf{B}$ and the charge of the ion q is known, the mass of the ion can be calculated directly from its free cyclotron frequency ν_c using equation (4). To determine the magnetic field strength $\mathbf{B}$ with high accuracy, a reference ion with well-known properties like $^{12}\mathrm{C}^{n+}$ is often used. By measuring its free cyclotron frequency in the same magnetic field the magnetic field strength can be calculated from the mass and charge of the reference ion.

2.3 Principle of Ion Detection and Motion Cooling

There are different techniques to measure the eigenfrequencies of a trapped ion [18, 19]. This bachelor thesis concentrates on a non-destructive detection method, that is based on the detection of mirror currents [20–22].

Currently, the PENTATRAP experiment measures the axial frequency ν_z of the charged particle in the trap directly, while both the modified cyclotron frequency ν_+ and the magnetron frequency ν_- are measured through sideband coupling [23, 24].

While oscillating between the end caps of the trap, the ion induces alternating image charges in the trap electrodes leading to an oscillating current I_z in an attached circuit. The induced current causes a voltage drop U_{signal} over the circuit's impedance $Z(\nu_z)$. The detected signal U_{det} is a superposition of the thermal noise U_{noise} and the voltage drop over $Z(\nu_z)$ [7]

$$U_{det} = U_{noise} + U_{signal} = U_{noise} + Z(\nu_z) \cdot I_z. \tag{9}$$

To get a good signal quality, a high signal-to-noise-ratio is needed. According to equation (9) this requires a preferably high impedance $Z(\nu_z)$. In practice, this is implemented using a resonant circuit which can be represented as a parallel

RLC-circuit (figure 3) with a resonance frequency [25]

$$\nu_0 = \frac{1}{2\pi\sqrt{LC_{tot}}},\tag{10}$$

where L is the inductance of the coil and C_{tot} the total capacitance of the resonant circuit resulting from the trap capacitance C_T, the intrinsic coil capacitance C_L and a parasitic cable capacitance C_C [7]:

$$C_{tot} = C_T + C_L + C_C.\tag{11}$$

The effective resistance R_{eff} [7] of the RLC-circuit is maximal for the resonance
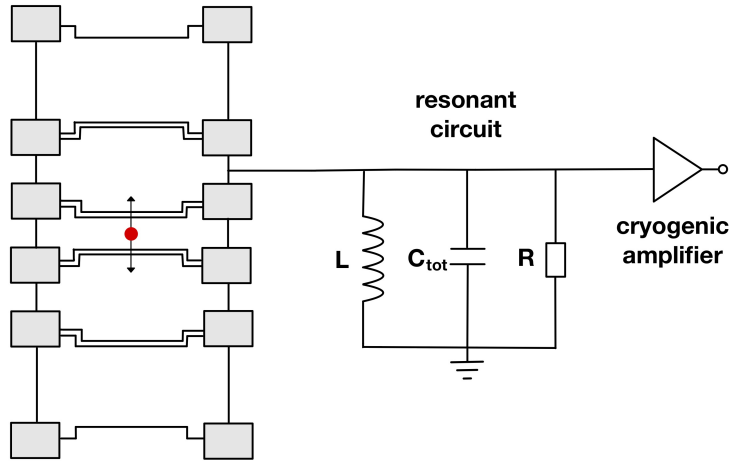
Figure 3: Axial resonator depicted as a RLC-circuit. To measure the axial frequency ν_z the resonator is connected to the correction electrode or the end cap electrode of a Penning trap. A cryogenic amplifier is used to preamplify the induced signal. The whole setup is cooled down to $4.2\,\mathrm{K}$. The figure is based on Figure 4 in [19].

frequency ν_0 [25] and can be calculated using

$$R_{eff} = 2\pi\nu_0 \cdot L \cdot Q.\tag{12}$$

The Q-factor of the system is defined as the ratio between the total energy stored in the resonant circuit and the amount of energy lost due to dissipation

after one oscillation [26].

Connected to the resonator is a cryogenic amplifier. To minimise any thermal noise, that can be modeled by the Johnson-Nyquist noise [27, 28], both the resonator and the amplifier are cooled down to a cryogenic temperature of $4.2\,\mathrm{K}$. The axial frequency ν_z can be easily adjusted through variation of the applied trap voltage U_0. For optimal detection it is important that $\nu_z = \nu_0$. The cryogenic amplifier reads out the detected signal and preamplifies it. At room temperature the signal then gets amplified again and detected with an FFT-analyzer that uses Fast Fourier Transformation to obtain a frequency spectrum [7]. The typical frequency spectrum of a resonator has a peak around the resonance frequency ν_0. If an ion is in the trap and its motion frequency is near the resonance frequency, a peak can be observed on top of the resonance spectrum. If the ion motion is thermalised, the motion frequency can be seen as a dip [19]. Figure 4 illustrates schematically how this looks like.
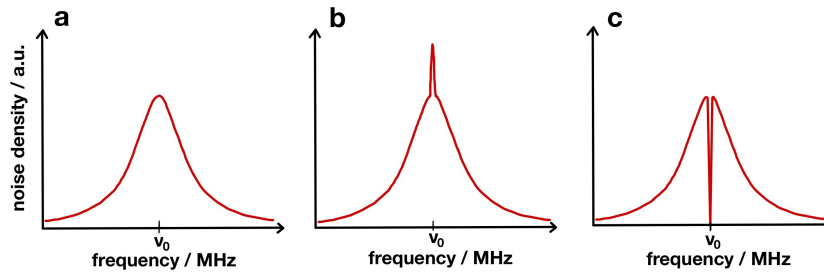
Figure 4: Schematic depiction of a frequency spectrum of a resonant circuit (a) without, (b) with, and (c) with a thermalised ion in the trap. This figure is based on Figure 4 in [19].

Other than for the direct measurement of the axial frequency ν_z the resonator is also used for "cooling" of the axial motion, i.e. for reducing the amplitude of the axial motion.

The voltage between the end cap electrodes and the ring electrode induced by the axial oscillation of the ion creates a small electric field near the center of the trap. This produces an electric force opposite to the axial motion of the ion, which damps the axial oscillation by decreasing the kinetic energy of the ion [15]. If $\nu_z = \nu_0$, the dissipation of the ion's kinetic energy into the RLC-circuit

is maximized [18, 29]. The energy decay is exponential and has a characteristic cooling constant τ_{cool} [30]:

$$\tau_{cool} = \frac{d_0^2 m}{q^2} \cdot \frac{1}{R_{eff}}.$$ (13)

The radius or amplitude of an eigenmotion are linked to a specific motional temperature $T_{\pm,z}$ via the kinetic energy

$$E_{kin,\pm,z} = \frac{1}{2}mv_{\pm,z}{}^2 = \frac{1}{2}m\omega_{\pm,z}^2 r^2 = \frac{1}{2}m(2\pi\nu_{\pm,z})^2 r^2 = \frac{1}{2}k_B T,$$ (14)

where k_B is the Boltzmann constant. The axial motion of the ion, being directly coupled to the cryogenic detection circuit, can be directly cooled down to the temperature of the resonator [31], in this case $4.2\,\mathrm{K}$.

The radial motions like the modified cyclotron motion with frequency ν_+ are cooled indirectly through side band cooling [32–34]. The achievable motion temperature T_+ depends on both frequencies ν_z and ν_+ and is higher than T_z by a factor of $\frac{\nu_+}{\nu_z}$ [30, 31]:

$$T_+ \approx \frac{\nu_+}{\nu_z} \cdot T_z.$$ (15)

Since the axial frequency is much smaller than the modified cyclotron frequency (see equation 7) this factor can be rather high. To control energy-dependent shifts of the eigenfrequencies [35, 36] and achieve high precision measurements, it is important to cool down the ion motions as much as possible [31].

At the PENTATRAP experiment a mass measurement of the pair $^{133}\mathrm{Cs}^{44+}$ and $^{12}\mathrm{C}^{4+}$ is planned for the foreseeable future. The expected eigenfrequencies for this measurement are around $\nu_+ \approx 35\,\mathrm{MHz}$ and $\nu_z \approx 0.5\,\mathrm{MHz}$, which would result, according to equation (15), in a cyclotron motion temperature of $T_+ \approx 300\,\mathrm{K}$. To achieve measurements with a relative precision of 10^{-11} it is desirable to reduce the temperature of the cyclotron motion.

2.3.1 Direct Measurement of ν_+

It is possible to measure the modified cyclotron frequency ν_+ directly using a cyclotron resonator (figure 5). In order for ν_+ to induce a detectable image current, the ring electrode is split into two halves [29, 37]. One of the halves is connected to a resonator. Since the modified cyclotron frequency cannot be as

easily adjusted as the axial frequency, varactor diodes are used to finetune the resonance frequency ν_0 to match the modified cyclotron frequency ν_+. Together with a cryogenic amplifier this setup is used to measure the modified cyclotron frequency ν_+ using the same detection principle already described in chapter 2.3.
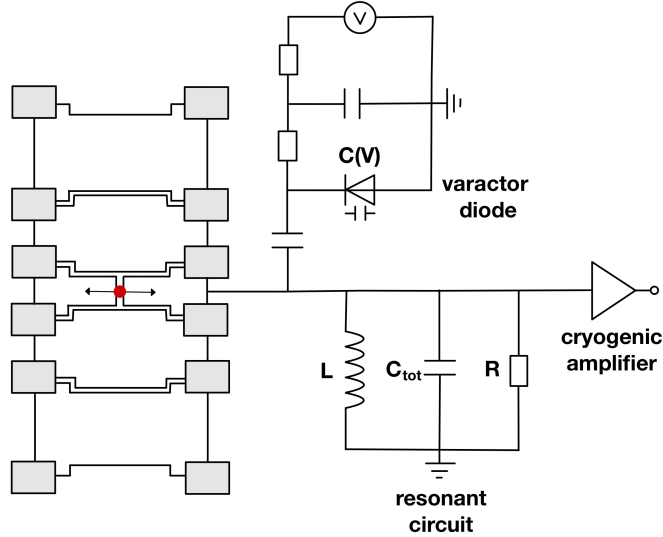
Figure 5: Cyclotron resonator depicted as a RLC-circuit. To measure the modified cyclotron frequency ν_+ the resonator is connected to the split ring electrode (RE) of a Penning trap. A cryogenic amplifier is used to preamplify the induced signal. A varactor diode is used to tune the resonance frequency. The whole setup is cooled down to $4.2\,\mathrm{K}$. The figure is based on Figure 4 in [19].

For the direct measurement of the frequency, the cooling constant should be bigger than the duration of the measurement. Therefore, a cooling constant of $\tau_{cool} = 100\,\mathrm{s}$ is reasonable. Using equations (12) and (13) a corresponding Q-factor can be calculated with

$$Q = \frac{d_0^2 m}{q^2} \frac{1}{2\pi\nu_{res} \cdot L \cdot \tau_{cool}}. \tag{16}$$

For $^{133}\mathrm{Cs}^{44+}$ with $L \approx 0.6\,\mu\mathrm{H}$ and $d_0 = 10\,\mathrm{mm}$ this would result in $Q_{min} = 34$, while for $^{12}\mathrm{C}^{4+}$ this renders $Q_{min} = 368$. Although a large cooling constant reduces the required Q-factor, a too small Q-factor results in a very low signal-to-noise ratio of the detection system. To ensure a good detection of the signal,

it is highly desirable to have a Q-factor larger than 500.

2.3.2 Direct Cooling of ν_+

Since sideband cooling is not efficient enough, the cyclotron resonator can be used to cool the ion motion without measuring it directly. Like in section 2.3.1, the electrodes need to be split and varactor diodes can be used to adjust the resonance frequency ν_0. A cryogenic amplifier is not needed. The cooling works according to the same principle already described in section 2.3.

Since the cooling process should happen very quickly, the cooling constant τ_{cool} needs to be small enough. The corresponding Q-factors for $^{133}\text{Cs}^{44+}$ and $^{12}\text{C}^{4+}$ for different cooling constants can be calculated using equation (16). The results are summarised in table 1. The cooling constant can be increased even more to lower the Q-factor, but still needs to stay small enough, so that the cooling process still happens fast enough and the duration of the measurement is not unnecessarily prolonged. Since both ion frequencies will be measured in the same trap [6], the higher Q-factor is the one that should be aimed for when constructing the detection system.

Table 1: Corresponding Q-factors for $^{133}\text{Cs}^{44+}$ and $^{12}\text{C}^{4+}$ for different cooling constants.

τ_{cool}	$1\,\text{s}$	$5\,\text{s}$	$10\,\text{s}$
Q-factor for $^{133}\text{Cs}^{44+}$	3369	673	337
Q-factor for $^{12}\text{C}^{4+}$	36779	7356	3678

11

3 Design and Characterisation of the Cyclotron Resonator

In this chapter the design and material choices of the cyclotron resonator are discussed. Section 3.1 describes the boundary conditions set by spatial limitations in the PENTATRAP experiment, while section 3.2 discusses the different wire materials that are used to construct the coil. In the last section 3.3 several measurements are summarised to determine a suitable coil size and winding number.

3.1 Boundary Conditions and Design

As discussed in chapter 2.3, the cyclotron resonator has to be placed inside a cryogenic environment to cool the ion motion efficiently and determine the eigenfrequency. The PENTATRAP experiment has limited space in the cryogenic insert, which is immersed in the cold bore of the superconducting magnet. For simplicity, the coils for the cyclotron resonator will be placed in the same type of housing as the already installed axial resonator. The housing is made from copper and is composed of three parts: an open body with cylinder shaped cutouts, which deliver space for up to six coils and two lids with several small holes to enable further electric connections. The dimensions are approximately 11.6 cm by 12.6 cm by 10.2 cm. The cylindrical cutouts are arranged in two planes and have a diameter of 48 mm each. Since the trap setup can only be taken out of the magnet during measurement downtime, the resonator tests were carried out in a separate lab using a coldhead. A smaller version of the copper-housing with room for only three coils was used for most of the measurements at cryogenic temperature, because the coldhead offered limited electrical connections. The dimensions of the small copper-housing including the lids are roughly 11.6 cm by 12.6 cm by 5.7 cm.

Just like the axial resonators of the PENTATRAP experiment [31], the cyclotron resonators, that were built and tested within this thesis work, have a toroidal geometry (see figure 9). This has the advantage, that the magnetic field lines of the coil are ideally confined inside the torus and there should be less losses inside the copper-housing compared to linear or planar coils. For simplicity it may be assumed, that any decrease of the Q-factor mainly originates from losses in the wire and the insulating material of the torus. Further details on

the choice of wire can be found in chapter 3.2.

In the beginning of the bachelor thesis work several parts were designed using the CAD-software SolidWorks to centre and fixate the coils inside the copper-housing. Also different sizes of toroids varying in diameter and width were designed and tested to be used as the core of the coil. All components are made from polytetrafluoroethylene (PTFE) and were manufactured in the workshop at MPIK.

Two cylindrical blocks ensure the proper placement of the coil at the vertical centre inside the housing. Several holes, matching the ones on the housing-lid, were added. During the measurements in the coldhead, the PTFE-parts are cooled down to cryogenic temperatures and therefore contract. To ensure enough thermal contact between the housing and the coil, the PTFE-blocks were made slightly taller (about $1\,\mathrm{mm}$) than needed. When closing both lids (top and bottom), the PTFE-blocks are firmly pressed onto the coil, ensuring a good connection to the housing, even at cryogenic temperatures.

For later measurements with thicker wire, the PTFE-blocks were shortened by a few millimeters. Small disks with a thickness of $0.5\,\mathrm{mm}$ each could then be added, when measurements with smaller wire were performed.

Two different designs were established to centre the coil between the PTFE-blocks. Both designs were implemented and used to perform measurements. A constructional drawing can be seen in figure 6. In the first version, one or two PTFE-rings, depending on the thickness of the coil, are placed around the coil. Small sticks, also made from PTFE, can be plugged into the ring to centre the coil and ensure the same distance to the copper-housing all around. The length of these sticks varies for different coil sizes. In the second version, a small cylinder-shaped attachment is added onto the centre of the PTFE-blocks. When the coil is put between two blocks, the attachment fits right in the middle of the coil and keeps it centred. Small PTFE-rings can be used to broaden the attachment if bigger coils are used.
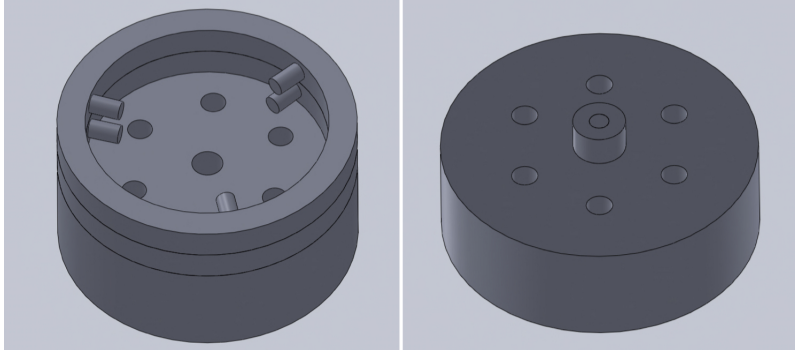
Figure 6: A constructional drawing of the lower halves of the PTFE-parts used to centre and fixate the coil inside the copper-housing. Left: Version one, where rings and sticks are placed around the coil. Right: Version two, where the coil is placed onto an additional ring in the middle.

While version two is a little bit simpler and easier to handle, the hole in the middle of the PTFE-block is closed, so that the small attachment can be added in the centre of the PTFE-block. Both ends of the wire of the coil need to be routed through different holes off-centre. Depending on the number and arrangement of the coil windings, the wire would overlap and be pressed onto the windings. If the isolation around the wire is not good enough and the wire routing is not handled carefully, this can cause a short circuit, thus altering the coil properties. In version one there is still an open hole in the middle of the PTFE-block. When routed through there, the wires don't overlap with other windings, thus decreasing the risk of a short circuit.

3.2   Wire-Material

With the assumption that the primary restriction is the resistance of the coil wire R_{coil}, the effective resistance R_{eff} can be approximated with [38]

$$R_{eff} \approx \frac{4\pi^2 \nu_0^2 L^2}{R_{coil}}, \tag{17}$$

where L is the inductivity of the coil and ν_0 the resonance frequency. It is then possible to estimate the quality factor of the resonator from equation (12) [38]:

$$Q \approx \frac{2\pi\nu_0 L}{R_{coil}}. \tag{18}$$

14

When dealing with frequencies in the range of a few MHz, it becomes necessary to consider the influence of the skin effect. The skin effect characterizes the distribution of the current density within a conductor carrying an alternating current (AC), where the highest density is observed at the surface and decreases exponentially towards the center. As a result of that, only a narrow outer layer of the conductor actively contributes to the total resistance of the coil [38]. If the electric resistivity ρ [Ω·m] and the magnetic permeability μ [$\frac{H}{m}$] of the conductor is known, the skin depth is given by [39]

$$\delta = \sqrt{\frac{2\rho}{\omega\mu}} \tag{19}$$

with ω being the angular frequency of the current flowing through the conductor. The resistivity at cryogenic temperatures is material dependent and is characterised through the residual resistance ratio

$$RRR = \frac{\rho(300K)}{\rho(0K)}. \tag{20}$$

The resistance of the coil wire can be calculated as

$$R_{coil} = \frac{\rho l_w}{A_w} \tag{21}$$

with l_w being the wire length and A_w the conductive wire cross section that can be calculated with the wire diameter d_w using [38]

$$A_w = \pi d_w \delta. \tag{22}$$

With a combination of equations (18), (21) and (22), a corresponding Q-factor, can be calculated with

$$Q = \frac{2\pi^2 d_w \delta_{4K} \nu_0 L}{l_w \rho_{4K}}. \tag{23}$$

For most measurements a coil made from Cu-wire of 99.99% purity with a diameter of 1.0 mm manufactured by ADVENT Research Materials Ltd. was used. Since this is a type C110 oxygen-free high thermal conductivity (OFHC) wire, it is characterised by $RRR \approx 100$ rendering $\rho_{4K} = 1.956 \cdot 10^{-10}$ Ω·m [40]. Since we don't have any detailed specifications from the manufacturer, the RRR-value is simply a guess based on the description of the wire as a type C110 and OFHC. With a skin depth of $\delta_{4K} = 1.68$ µm a maximal Q-factor of approximately 4400

15

can be calculated using equation (23) for a coil with L=0.6 μH and l_w=0.566 m.

Equation (23) only considers losses within the wire and although this is the main limiting factor, in reality there are additional losses [38], e.g. dialectric losses in the PTFE-body of the torus, which will lead to a smaller Q-factor of the resonant circuit by a factor of about 2.5 (see also chapter 4.1). It is also possible, that the RRR of the Cu-wire is overestimated. The RRR for type C110 wire ranges from 50-100 [41] and could thus be much lower.

During this bachelor thesis, several measurements were performed using Cu-wire and NbTi-wire of different purity and thickness. A summary of all used wire materials and their properties can be seen in table 2.

Table 2: Material and properties of all wires that were used for testing different resonator coils. Perfluoroalkoxy alkanes (PFA) are fluoropolymers with similiar properties as PTFE. For further details see text.

material	bare diameter	insulation	insulated diameter
Cu, 99.9%	0.5 mm	-	-
Cu, 99.95%	1.0 mm	-	-
Cu, 99.99%	1.0 mm	-	-
Cu, 99.99%	2.0 mm	-	-
NbTi	0.075 mm	PFA	0.28 mm
NbTi	0.7 mm	-	-

In order to reduce electrical losses, a superconducting material like niobium-titanium (NbTi) can be used instead. NbTi is a type II superconductor with a critical temperature of $T_C = 9.5$ K and an upper critical magnetic field $B_{C_2} = 14$ T [42]. Since the resonator will be cooled down to 4.2 K, NbTi shows superconductive characteristics; its magnetic permeability is approaching zero and should thus reduces the skin effect and minimize losses caused by the electrical resistance of the wire.

However, the surface resistance of superconducting materials like NbTi increases in general, when they are put inside a magnetic field due to the flux-flow-resistance. Above the lower critical magnetic field B_{C_1} the superconductor is in the so called Shubnikov-phase, where the outer magnetic field can force its way

into the superconductor through magnetic flux lines. If a current runs through the superconducting wire, a Lorentz force is generated and affects the normal conducting component of the magnetic flux lines. The movement of these flux lines leads to further losses [43].

For NbTi the lower critical magnetic field is $B_{C_1} = 24\,\mathrm{mT}$. Since the PENTATRAP experiment is operated inside a magnetic field of $7\,\mathrm{T}$ [6], the surface resistance of NbTi is expected to increase. In [44] it is even suggested, that the surface resistance of a NbTi resonator operated inside a strong magnetic field $>1\,\mathrm{T}$ would be higher at a resonance frequency of $35\,\mathrm{MHz}$ compared to the surface resistance of copper with RRR=140. Therefore, it is recommended to use copper resonators for measurements in higher magnetic fields and at higher resonance frequencies [44].

In the course of this bachelor thesis all measurements are performed without the presence of an external magnetic field. The resistance of the resonator is definitely expected to increase inside the PENTATRAP setup, qualitative measurements on the extend of the decrease of Q-factor were not performed yet, but will be carried out in the near future.

3.3 Measurements to Determine the Coil Design

The first measurements to find the optimal coil design were performed with coils made from Cu-wire with a diameter of $0.5\,\mathrm{mm}$ and a purity of 99.9%. For different torus sizes one coil each was constructed with N windings wound as tightly as possible and one with N windings evenly spread across the whole torus. An example pair can be seen in figure 7. The inductance and the capacitance of the coils were determined to get an idea of what design is better suited.

The self capacitance C_R of a resonant circuit can be experimentally determined from the ratio of the free resonance frequency $\nu_{0,free}$ and the resonance frequency $\nu_{0,C}$ you measure, when the resonator is connected to an additional capacitance C. With equation (10) C_R can be calculated using [45]

$$C_R = \frac{C}{(\frac{\nu_{0,free}}{\nu_{0,C}})^2 - 1}. \tag{24}$$

17
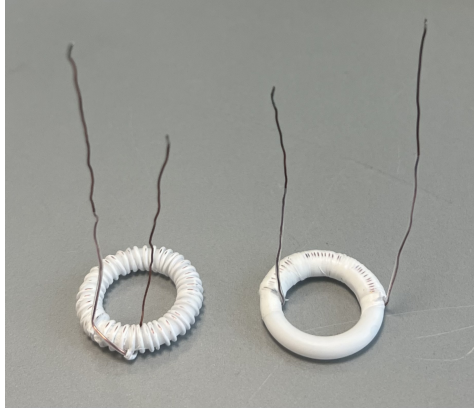
Figure 7: Example of a coil with an evenly wire distance (left) and of a tightly (right) wound coil. The inner radius of the depicted rings is 10 mm, the outer radius is 15 mm. Both coils have 41 windings. The picture was taken after the measurements were performed. When taking the coils out of the Cu-housing the PTFE-insulation was slightly damaged.

With equation (10) it is then possible to calculate the inductance L from the measured and calculated values for C_R and $\nu_{0,free}$

$$L = \frac{1}{4\pi^2 C_R \cdot \nu_{0,free}^2}. \tag{25}$$

To measure the resonance frequency of the resonator, the coil is placed inside the copper-housing and both wire ends are routed through the top lid. The "cold" wire end of the coil is grounded, while the "hot" wire end either remains free or is soldered to a capacitance C. A ZNL3 Vector Network Analyzer (VNA) from the company "Rohde & Schwarz" is used to readout the resonance frequency using a small excitation signal. The signal from and to the VNA is inductively coupled to the "hot" wire end. A picture of this setup can be seen in figure 8.

It is important that the isolation of the "hot" end is well done and the wire has no direct contact to the copper-housing. Most wires used in this thesis are not insulated. The insulation layer is added manually during or after the winding process of the coil with PTFE-tape and PTFE-sleeves. All capacitors used during the measurements are from the "High Q/Low ESR ceramic Capacitors Designer Kit" by Johanson Technology.
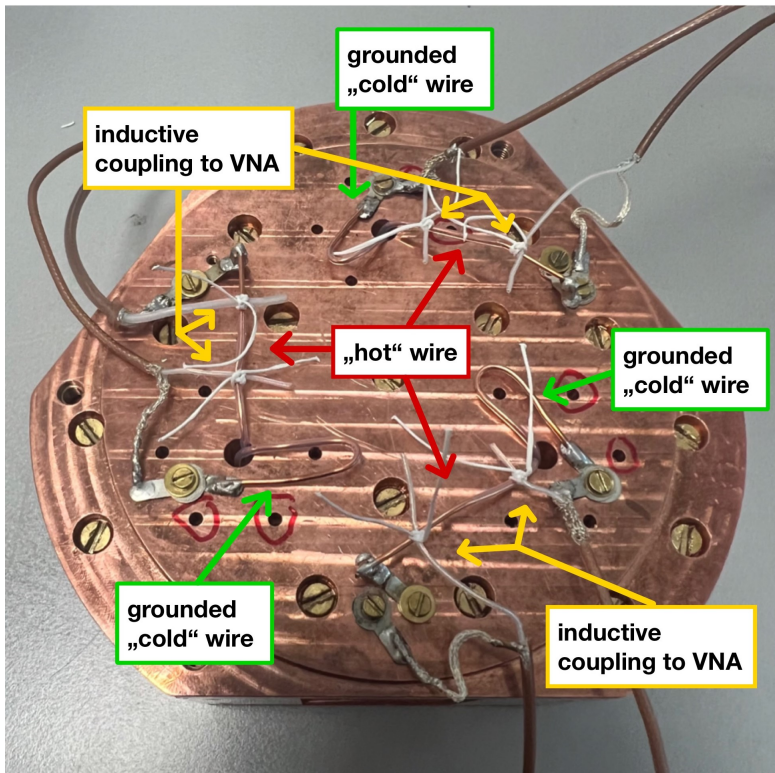
Figure 8: The setup to measure the inductance L and the capacitance C_R of three resonant circuits. The "cold" wire ends (green) are grounded, while the "hot" wire ends (red) are each soldered to a capacitance C. The signal from and to the Vector Network Analyzer (VNA) is capacitively coupled (yellow), the corresponding wires are isolated and tied to the "hot" wire with PTFE-tape.

The results of the L and C measurements can be seen in table 3 and 4.

A coil with a small capacitance and a high inductance is desirable and should deliver the highest Q-factor. Therefore the smallest ring with tight windings all around should be best. That this is not the case here can be seen in table 3 and traced back to irregularities and errors during the winding process. The relatively thick copper-wire compared to the small dimensions of the coil itself makes it hard to form and distribute the windings evenly.

In general the capacitance is bigger and the inductance smaller for evenly distributed windings. For larger torus sizes, both the capacitance and inductance

Table 3: The experimentally determined inductance L and capacitance C_R of the resonant circuit. All coils have an intrinsic diameter of 5 mm and a winding number of N=41. For the smallest coil a tight distribution of wires is equivalent to an even distribution of wires if one wants to keep the windings in a single layer, so there is no entry for an even winding distribution.

winding distribution	inner radius of the toroid in mm	outer radius of the toroid in mm	L in µH	C_R in pF
	5	10	0.988	2.41
tightly	7.5	12.5	1.111	2.19
	10	15	1.163	2.21
	12.5	17.5	1.324	2.51
	7.5	12.5	1.036	2.60
evenly	10	15	0.843	3.70
	12.5	17.5	0.726	3.33

Table 4: The experimentally determined inductance L and capacitance C_R of the resonant circuit. All coils have an intrinsic diameter of 10 mm and a winding number of N=15.

winding distribution	inner radius of the toroid in mm	outer radius of the toroid in mm	L in µH	C_R in pF
	2.5	12.5	1.041	2.51
tightly	5	15	1.274	2.57
	7.5	17.5	1.210	2.63
	2.5	12.5	0.878	3.56
evenly	5	15	0.678	3.53
	7.5	17.5	0.603	3.57

increase for tightly winded coils. Because the windings are not evenly distributed the ring shape of the coil is opened up and the magnetic field lines are no longer confined inside the torus causing edge effects. If the windings are done too tightly, the insulation layer (PTFE-tape) could be damaged, leading to a possible short circuit due to wires touching especially at the smaller inner diameter of the coil. A lot of measurements done in the early stages of this thesis did not show any results because of short circuits. To prevent this from happening, to reduce the overall chance for errors, and because the overall winding process is easier, mainly coils with evenly distributed windings were used for further measurements.

Since thicker Cu-wires will be used in the following measurements, the core with the bigger cross section (intrinsic diameter of 10 mm) was chosen, because otherwise the stiffness of the wire would lead to more winding irregularities. To compensate for little wire flexibility not the smallest, but the second smallest ring size was chosen with an inner radius of 5 mm and an outer radius of 15 mm. Simultaneously, coils made with thin NbTi-wire were made using the smallest

ring size with an inner radius of 2.5 mm and an outer radius of 7.5 mm. To improve the fixation of the wire around the torus shape and to better control the distribution of the windings a new design for the core of the coil was developed: a disk shape addition to the coil body with 48 evenly distributed holes to ensure confinement around the torus (see figure 9). The torus has an inner radius of 5 mm and an outer radius of 15 mm.
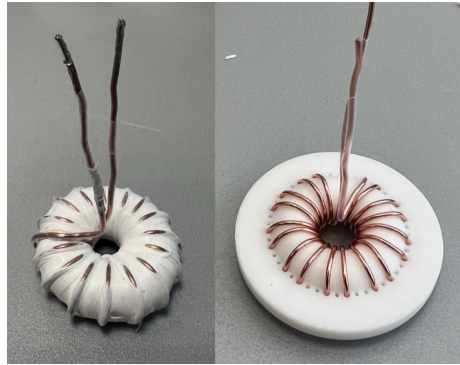

Figure 9: Picture of the initial (left) and the newly adapted (right) coil design. The picture of the adapted coil design was taken before the windings were fixated and insulated with PTFE-tape. The left coil with the initial design has not yet been adapted to a resonance frequency of 35 MHz, hence the coil has a winding number of $N=16$ instead of $N=18$.

The inductance of the resonant circuit needs to be adapted such that its resonance frequency matches the cyclotron frequency of the ion of interest as good as possible. This was done experimentally via the Q-factor measurements described in chapter 4. Through variation of the number of the coil windings a resonance frequency of around 35 MHz was obtained, while the resonant circuit was connected to a capacity of $C=20$ pF, which is about the same size as the parasitic capacitance of one of the traps at the PENTATRAP experiment and can therefore act as a representation of a trap during the coldhead tests. For the chosen coil geometry this results in $N=18$. Between both wire ends of the coil a small free space of approximately 1 cm corresponding to five holes around the torus was left. This is mainly important for coils made from NbTi, where two small pieces of Cu-wire need to be soldered to both NbTi-wire ends and fixated to ensure a good enough thermal connection to the wire, since NbTi is a rather bad heat conductor [44].

4 Q-factor Measurements

This chapter explains how the Q-factor of the resonator is measured. The results for different measurements with coils made from Cu-wire or NbTi-wire are summarized in section 4.1 and 4.2.

To determine the Q-factor of the resonant circuit experimentally, the same setup as described in chapter 3.3 is used. The coil is placed inside the copper-housing, the "cold" wire end is soldered to the lid and thus grounded, while the "hot" wire end is connected to a capacitance. The signal from and to the VNA is capacitively coupled and read out via overlapping of insulated wires. The so called -3dB bandwidth of the resonance signal is the full width half maximum FWHM in log-scale and defines the bandwidth where the power is at least half of the value at resonance (illustrated in figure 10). The -3dB bandwidth is measured and used to calculate the Q-factor according to [38, 45]

$$Q = \frac{\nu_0}{\Delta\nu_{-3dB}}.$$ (26)

The narrower the signal is, the bigger is the Q-factor at a fixed frequency ν_0. Additionally a high signal-to-noise-ratio is desirable.
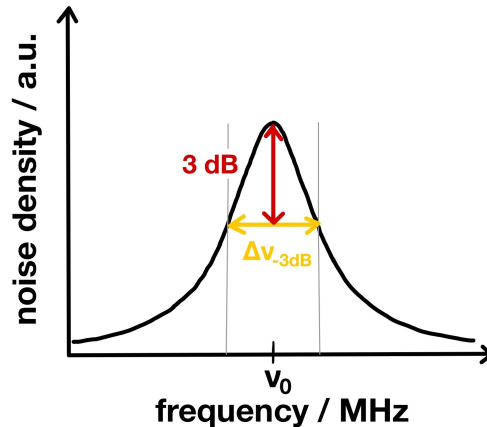

Figure 10: Schematic depiction of the -3dB bandwidth (yellow) of a resonance spectrum. The noise density is depicted in log-scale.

Figure 11 shows an example of how this typically looks like on the VNA. The VNA can be set up such, that the -3dB bandwidth of the resonance spectrum

is automatically determined and the Q-factor can be read out directly from the display.
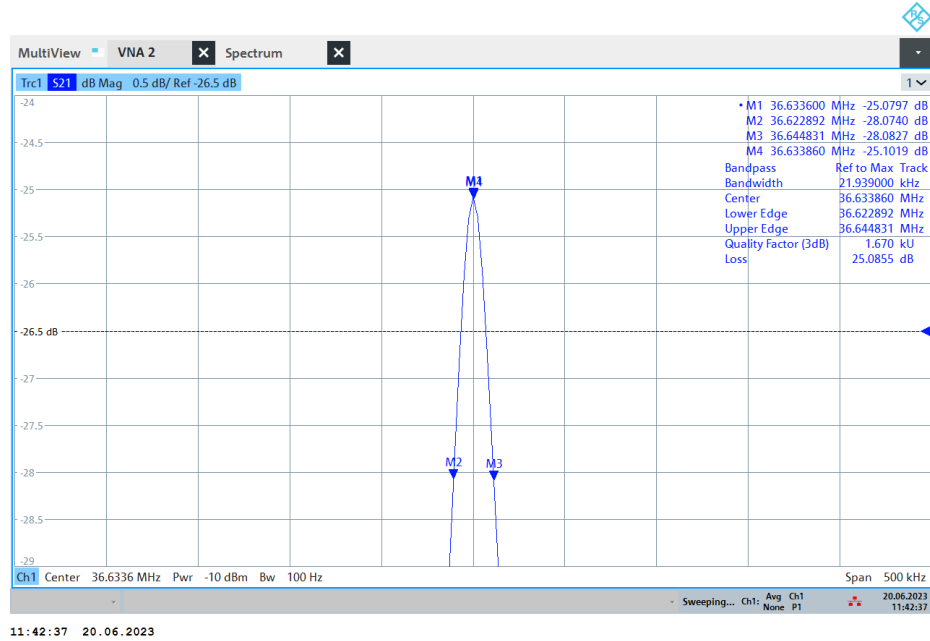
Figure 11: Screenshot of a typical resonance peak displayed on the VNA. Markers are used to determine the resonance frequency and the -3dB bandwidth of the signal. The Q-factor is automatically calculated and displayed on the top right.

4.1 Q-factor Measurements with Cu-Wire

Several Q-factor measurements with coils made from different Cu-wires were performed. A summary of the results is given in table 5. All measurements were performed once at room temperature and once at a cryogenic temperature of $4.2\,\mathrm{K}$ in the coldhead. A small shift of the resonance frequency of less than $0.5\,\mathrm{MHz}$ can be observed, when the resonant circuit is cooled down. Overall we were able to reach Q-factors up to almost 1700. The highest Q-factors of 1680 and 1670 were reached with coils made from 1 mm Cu-wire with a purity of 99.99%.

Looking at the different wire sizes, we would expect the thickest to be the best, since according to equation (23) the Q-factor is directly proportional to

23

Table 5: A summary of the results from the Q-factor measurements where several coils made from different types of Cu-wire were tested. For more details see text.

wire	coil design	N	C	ν_0 (300 K)	Q (300 K)	ν_0 (4.2 K)	Q (4.2 K)
0.5 mm, 99.9%	simple, evenly	16	1 pF	97.30 MHz	160	97.28 MHz	500
1 mm, 99.95%	simple, evenly	16	1 pF	87.63 MHz	370	87.93 MHz	1660
				91.65 MHz	367	91.75 MHz	1572
				91.48 MHz	353	91.61 MHz	1371
1 mm, 99.99%	simple, evenly	16	1 pF	91.07 MHz	382	91.42 MHz	1600
				92.71 MHz	373	92.59 MHz	1500
				89.69 MHz	377	89.64 MHz	1460
			33 pF	33.80 MHz	256	33.57 MHz	1430
1 mm, 99.99%	simple, tightly	8	1 pF	120.44 MHz	448	120.97 MHz	1680
				118.75 MHz	437	118.40 MHz	1440
			20 pF	51.26 MHz	324	51.05 MHz	1637
				52.10 MHz	338	51.93 MHz	1669
1 mm, 99.95%	new, evenly	18	20 pF	37.77 MHz	285	37.47 MHz	1391
1 mm, 99.99%	new, evenly	18	20 pF	38.19 MHz	290	37.83 MHz	1628
				35.48 MHz	285	35.14 MHz	1643
1 mm, 99.99%	new, evenly, with 3rd wire	18	20 pF	36.19 MHz	290	35.78 MHz	1670
				34.53 MHz	266	34.06 MHz	1627
				37.05 MHz	273	36.63 MHz	1670
2 mm, 99.99%	new, evenly	11	20 pF	57.66 MHz	325	57.52 MHz	1417

the wire diameter. Clearly the lowest Q-factors were reached from the coils made from the thinnest Cu-wire. The low Q-factor of coils made from 0.5 mm wire was expected due to the low purity of that particular wire. Contrary to the predictions the thickest Cu-wire has not the highest Q-factor. This can be explained due of the fact that the wire was too thick for these small dimension. There were a lot of irregularities, e.g. the windings were not evenly distributed all around, because there was simply not enough space at the inner side of the torus. Due to these imperfections the magnetic field lines are no longer fully confined inside the torus, leading to additional losses and thus to a reduced Q-factor.

Looking at the different wire purities, it is also no surprise that the purest Cu-wire has the highest Q-factor, since the skin effect is less restricting for copper with higher purity due to its smaller electric resistivity.

There were also measurements performed using tightly wound coils, but al-

though a maximum Q-factor of 1680 was reached, in general the difference to the Q-factors obtained with evenly wound coils is not significant. A specific Q-factor can slightly fluctuate between two independent measurements, even when the same coil is used, depending on the exact temperature of the resonant circuit and the connection to the VNA.

The implementation of the new coil core design (see figure 9) improved the reproducability of the Q-factor. Using the first and simpler core design, Q-factors bigger than 1600 were reached, but there were big fluctuation in the performance of in principal identical resonant circuits. With the new core design, every resonant circuit using a coil made with the 1 mm copper-wire with a purity of 99.99% reached Q-factors above 1600. Although the exact resonance frequency cannot be predicted, the resonance frequencies for different coils made from the same wire, with the same geometry and winding number all lay within 10% of each other.

4.2 Q-factor Measurements with NbTi-Wire

Another set of Q-factor measurements was performed using coils made from NbTi-wire. A summary of the results can be seen in table 6.
Since the frequency spectrum of a superconducting resonant circuit cannot be detected at room temperature, the resonance frequency ν_0 and the Q-factor were measured at $4.2\,\mathrm{K}$ in the coldhead.

To ensure a good thermal contact to the coil, two short pieces of Cu-wire are soldered to both wire ends of the NbTi-coil. A good thermal connection to the NbTi-wire is the most tricky part and probably the reason for the large variation of Q-factors. The Q-factor of NbTi-coils is not reliably reproducible and depends on the connection to the copper wires. Overall the same rules apply as before: thicker Cu-wires with high purity are best suited and result in higher Q-factors than thinner or low purity wires.

The Q-factor can also be improved with a different type of solder [44]. Using Sn96.5Ag3Cu0.5-solder instead of regular Sn60Pb38Cu2-solder improved the Q-factor by about 600 (corresponding to approximatly 16-20%). Additionally an attempt was made to weld the NbTi-wire to the Cu-wire with a Lampert PUK-5 argon-ion arc-discharge spot welder using the same welding technique described

Table 6: A summary of the results from the Q-factor measurements where different coils made from NbTi-wire were tested. For more details see text.

wire	coil design	N	C	ν_0 (4.2 K)	Q (4.2 K)
0.075 mm	simple, evenly	15	1 pF	73.32 MHz 74.80 MHz 72.57 MHz	1300 3000 1500
0.075 mm	simple, evenly	13	1 pF	86.88 MHz 87.35 MHz 95.59 MHz	2300 3000 2070
0.075 mm	simple, tightly, thin Cu-wire simple, tightly, thick Cu-wire	8	1 pF	124.17 MHz 119.90 MHz	1165 1850
0.075 mm	new, evenly	14	20 pF	44.00 MHz	2590
0.075 mm	new, evenly new, evenly, different solder	18	20 pF	32.10 MHz 34.05 MHz 34.40 MHz 32.20 MHz 32.76 MHz	3600 2840 3480 4240 4100
0.7 mm	new, evenly new, evenly, welded	14	20 pF	44.00 MHz 45.80 Mhz	2590 3030

in [46]. It was possible to create a small welded joint right before the soldered spot between the thicker NbTi-wire and a piece of 1 mm Cu-wire with a purity of 99.99%. Comparing the Q-factors measured before and after the welding, an increase of 440 can be observed (corresponding to approximately 17%).

The thicker NbTi-wire does also not result in higher Q-factors, again imperfections and irregularities of the coil windings are at fault. The wire was too stiff to form consistently arranged windings even with the new coil design. When comparing the NbTi-coils to the Cu-coils that have the same geometry and winding distribution, one can see that the resonance frequency of the superconducting resonant circuit is a little bit lower.

The highest Q-factor that was obtained was 4240. The used coil had 18 windings evenly distributed around the new design and was made from the PTA insulated thin wire. Two short pieces of Cu-wire with a diamater of 1mm and

99.99% purity were connected to the NbTi-coil with Sn96.5Ag3Cu0.5-solder.

5 Frequency Tuning with Varactor Diodes

The following chapter explains briefly why varactor diodes are needed. The possible tuning range and the influence of the varactor circuit on the Q-factor were determined for one and three varactor diodes. The results are discussed in section 5.1 and 5.2.

While the axial frequency of the trapped ion can be easily tuned via the applied trap voltage to match the resonance frequency of the detection system, the modified cyclotron frequency cannot be altered that way, since it would require a change in the magnetic field of the superconducting magnet, which is not easily possible. Since the total capacitance, especially of the connecting cable and the trap electrodes, are challenging to measure before with sufficient accuracy, it is beneficial to have some method of tuning the resonant frequency in-situ (see also chapter 4.1). In this case, varactor diodes are used to realize a voltage controlled oscillator (VCO), being the resonance circuit, to match the modified cyclotron frequency of a trapped ion. Varactor diodes are semiconductor devices that change their capacitance with an applied voltage, functioning as voltage-controlled capacitors. A diagram of the varactor circuit with the specific component properties can be seen in figure 12.

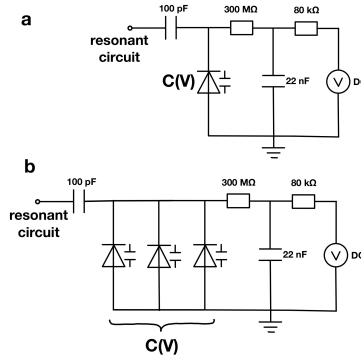**Figure 12:** Schematic diagram of the varactor circuit with one (a) or three (b) varactor diodes. The first capacitor with $100\,\mathrm{pF}$ is used to capacitively couple the varactor diode to the detection circuit. The $300\,\mathrm{M\Omega}$ resistance is used as a blocking resistance to "protect" the resonant circuit site from the huge filter capacitance and possible parasitic capacitances.

One or three varactor diodes are strongly coupled to the resonant circuit via a capacitor with $100\,\text{pF}$. Due to the additional losses in the varactor circuit, the Q-factor of the resonant circuit is decreased depending on the applied voltage.

The implementation of the varactor circuit into the whole setup of the detection system is shown in figure 5 and the experimental realisation of the varactor circuit can be seen in figure 13. The printed circuit board is screwed on top of the housing-lid. The wire ends are soldered to the board instead of directly onto the lid, the "cold" wire is grounded, while the "hot" wire is soldered to the coupling capacitor. The signal from and to the VNA is capacitively coupled to the "hot" wire. During the measurement, the corresponding cables are fixated with PTFE-tape. The varactor circuit board is connected to an external DC-voltage source. By varying the applied voltage, the capacitance of the varactor diode and thus the total capacitance of the resonant circuit changes and the resonance frequency is shifted.
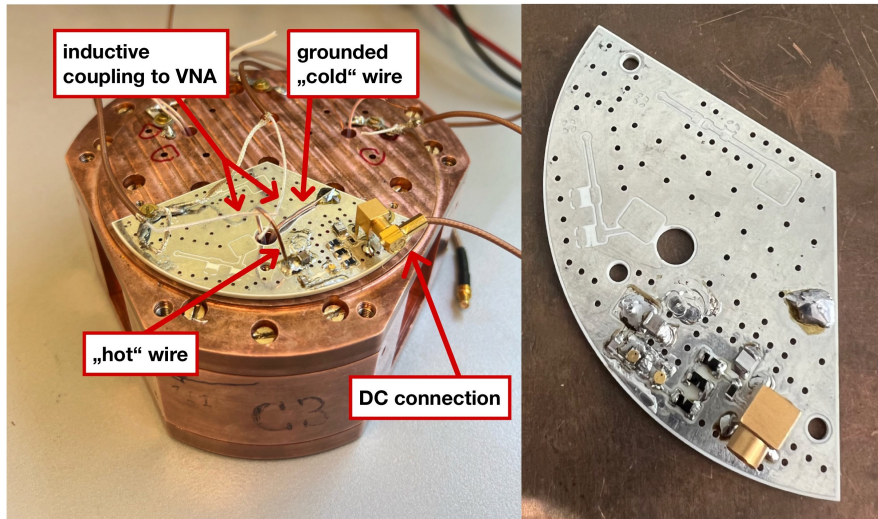
Figure 13: Experimental realisation of the varactor circuit. Left: Implementation of the varactor circuit; the printed circuit board is screwed on top of the housing-lid. The "cold" wire is grounded, while the "hot" wire is soldered to the coupling capacitor. The varactor circuit is connected to an external DC source. The signal from and to the VNA is capacitively coupled and read out. Right: Close-up of the board of the varactor circuit with three varactor diodes.

5.1 Frequency Tuning with one Varactor Diode

The following measurements were performed using one varactor diode to tune the resonance frequency. The properties of the used coil are summarized in table 7. The measurements were performed before the winding number and distribution of the coil was adapted to a resonance frequency of approximately 35 MHz when connected to a trap simulating capacitance of C=20 pF. The used coil had N=16 windings and the initial simple coil design. To still perform the measurements around the desired frequency range a capacitance of 33 pF instead of 20 pF was used, resulting in a Q-factor drop from 1600 to 1430. Since the newest coils all have a Q-factor above 1600 even when connected to a capacitance of C=20 pF (see chapter 4.1), the Q-factor during the frequency tuning with the new coils is expected to be higher than here depicted. Nevertheless, the relative variation is expected to be in the same range.

Table 7: Properties of the coils used for the frequency tuning measurements. The capacitance C_R and inductance L of the coil were calculated using equations (24) and (25). The free resonance frequency $\nu_{0,free}$ of the coil is 102.36 MHz.

wire	coil design	N	C	Q-factor	ν_0	L	C_R
1 mm, 99.99% Cu	simple, evenly	16	1 pF	1600	91.31 MHz	0.620 μH	3.90 pF
			33 pF	1430	33.80 MHz	0.636 μH	3.80 pF

The setup was cooled down do 4.2 K in the coldhead. The applied voltage was varied, while the resonance frequency and the Q-factor of the resonant circuit were measured with the VNA. The results can be seen in figure 14 and 15.

The Q-factor ranges from 1200 to 1470 resulting in a maximal Q-factor suppression of up to 18%. The resulting resonance frequency of the detection system depending on the voltage of the varactor diode ranges from 30.32 MHz to 32.22 MHz, therefore a tuning range of 1.90 MHz was achieved.
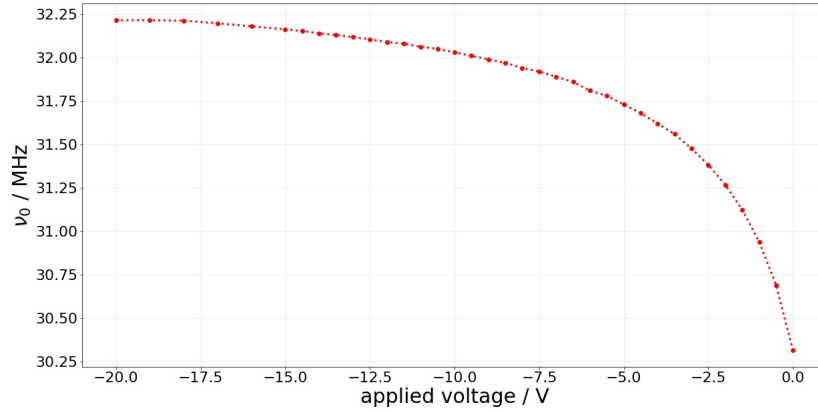
Figure 14: Resonance frequency of the detection system depending on the voltage of the varactor diode. One varactor diode was used for frequency tuning.
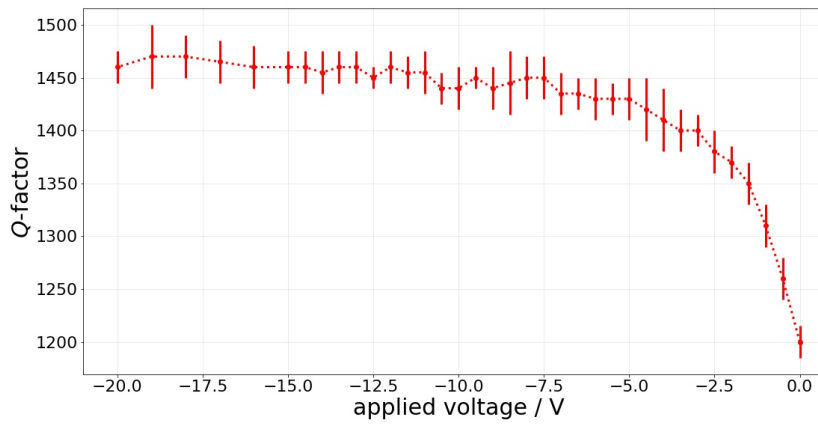

Figure 15: Q-factor of the detection system depending on the voltage of the varactor diode. One varactor diode was used for frequency tuning. The error bars result from fluctuations during the measurement.

5.2 Frequency Tuning with three Varactor Diodes

To increase the range of the frequency tuning, three varactor diodes were used instead. In the following the results of the measurements will be presented. The same basic setup and coil as before in 5.1 were used. The results can be seen in figure 16 and 17.
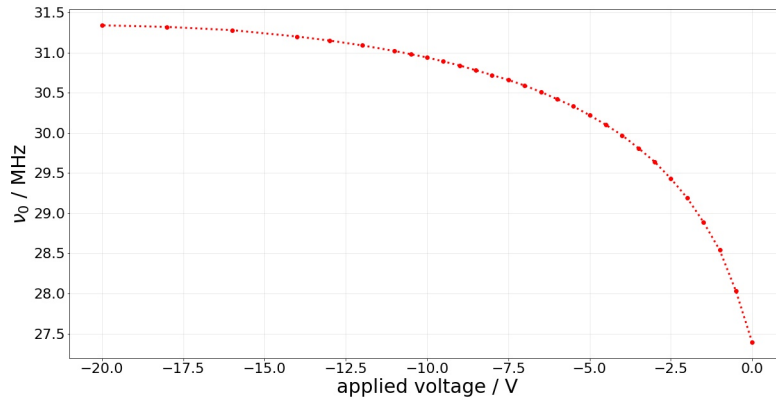

Figure 16: Resonance frequency of the detection system depending on the voltage of the varactor diodes. Three varactor diodes were used for frequency tuning.
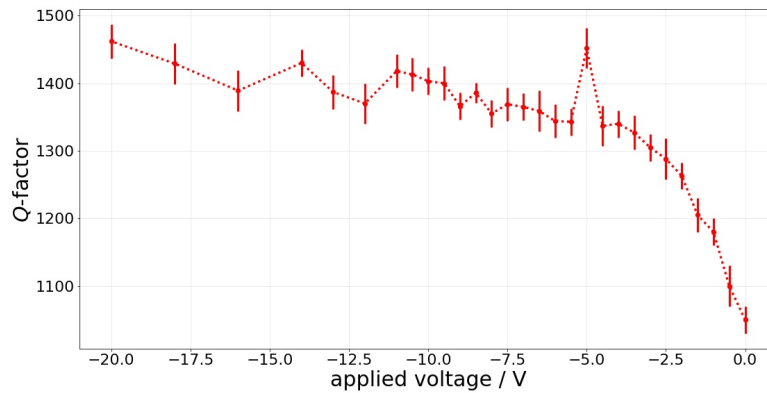

Figure 17: Q-factor of the detection system depending on the voltage of the varactor diodes. Three varactor diodes were used for frequency tuning. The error bars result from fluctuations during the measurement.

This time, the Q-factor ranges from 1050 to 1462 resulting in a maximal Q-factor suppression of up to 28%. The resulting resonance frequency of the detection system depending on the voltage of the varactor diode ranges from 27.39 MHz to 31.34 MHz, therefore the tuning range is 3.95 MHz. This is more than twice the tuning range achieved with one varactor diode.

Because the resonance frequency of the resonant circuit can only be controlled within approximately 10% (see chapter 4.1), this variation needs to be compensated for. For a targeted resonance frequency of 35 MHz a minimum tuning range of 3.5 MHz is needed. The achieved tuning range of 3.95 MHz is therefore sufficient.

6 Signal Detection with a Cryogenic Amplifier

The motion of the trapped ion induces a mirror current in the resonant circuit in the order of fA. The signal of the resonator is preamplified before leaving the cryogenic environment with a cryogenic amplifier, then amplified again at room temperature and finally detected with an FFT-analyzer [7]. Since the induced currents are so small, the cryogenic amplifier should have a high signal-to-noise-ratio. In this chapter the signal of the resonant circuit is detected with a cryogenic amplifier and the signal-to-noise-ratio is measured.

For the detection of the resonator signal an already existing amplifier was used. The amplifier has a similar design as the ALPHATRAP axial amplifier described in [5], its dimensions are 28 mm by 39 mm. A diagram of the amplifier circuit can be seen in figure 18.

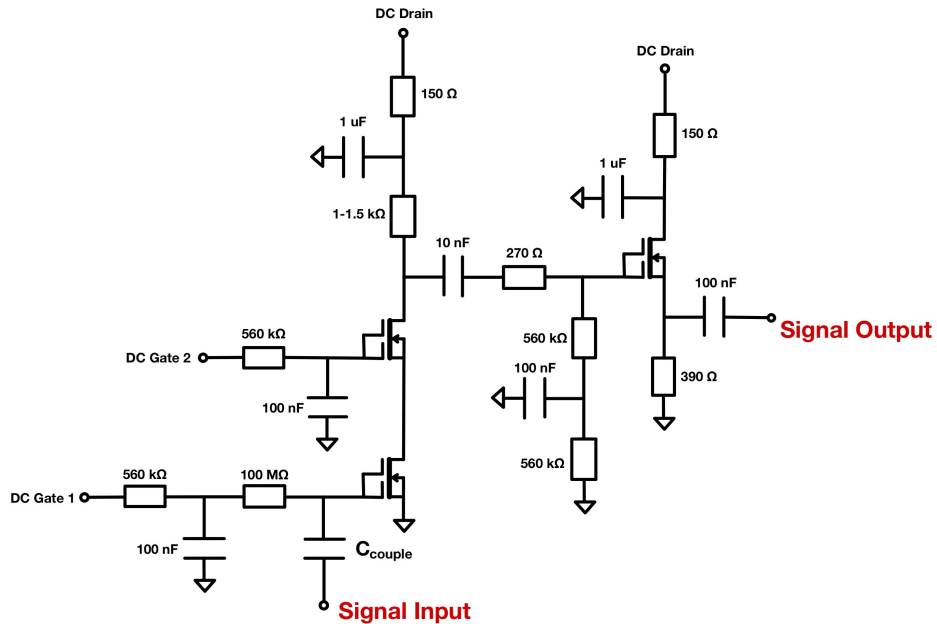
Figure 18: Schematic diagram of the amplifier circuit. For more details see text.

The circuit board of the amplifier is screwed onto the side of the copper-housing. A third wire was soldered to the "hot" wire of the resonator coil and routed

through a hole in the side of the Cu-housing. The amplifier then is capacitively coupled to the resonant circuit (see also figure 19). The addition of the third wire or rather the splitting of the "hot" wire alters the properties of the coil. A comparison of the properties of the same coil with and without the third wire can be seen in table 8.

Table 8: Coil properties with and without a third wire soldered to the "hot" wire. The used coil is made from $1\,\mathrm{mm}$ 99.99% Cu-wire, has the new coil design, N=18 and is connected to a trap simulating capacitance of $20\,\mathrm{pF}$. The capacitance C_R and inductance L of the coil were calculated using equations (24) and (25). The measurements were performed at room temperature.

3rd wire	$\nu_{0,free}$	C	$\nu_{0,C}$	L	C_R
$-$	$87.71\,\mathrm{MHz}$	$20\,\mathrm{pF}$	$35.56\,\mathrm{MHz}$	$0.838\,\mathrm{\mu H}$	$3.93\,\mathrm{pF}$
✓	$63.30\,\mathrm{MHz}$	$20\,\mathrm{pF}$	$34.90\,\mathrm{MHz}$	$0.724\,\mathrm{\mu H}$	$8.73\,\mathrm{pF}$

The following measurements were performed at cryogenic temperatures in the coldhead. The resonance signal without any additional excitation was read out with the amplifier. For the first measurement a coupling capacity of $18\,\mathrm{pF}$ was used. Because this resulted in a drastic suppression of the Q-factor of the resonant circuit, two more measurements were performed with smaller coupling capacitances. The results are summarised in table 9.

Table 9: Signal detection with an amplifier: Q-factor depending on the coupling capacitance. The first entry is the measurement of the coil without a coupling to the amplifier.

$C_{coupling}$	ν_0	Q-factor
$-$	$35.78\,\mathrm{MHz}$	1670
$18\,\mathrm{pF}$	$33.62\,\mathrm{MHz}$	290
$4.7\,\mathrm{pF}$	$34.27\,\mathrm{MHz}$	544
$1.95\,\mathrm{pF}$	$34.40\,\mathrm{MHz}$	860

The weaker the capacitive coupling is, the more does the detected resonance frequency approach the free resonance frequency of the resonant circuit and the

Q-factor is less suppressed. With a weak coupling capacitance of just $1.95\,\mathrm{pF}$ the resonator signal has a Q-factor of 860.

The amplifier was initially designed for much lower frequencies and is not optimised for our frequency range. There seems to be a feedback between the first and second transistor, resulting in the suppression of the Q-factor. To improve the performance of the amplifier, the design was adapted. A bigger circuit board was used and the transistors were placed as far away from each other as possible. The circuit itself was not changed. The new circuit plate fits perfectly onto the side of the bigger copper-housing, its dimensions are $28\,\mathrm{mm}$ by $78\,\mathrm{mm}$. The general measurement setup and a close-up of the new amplifier can be seen in figure 19.
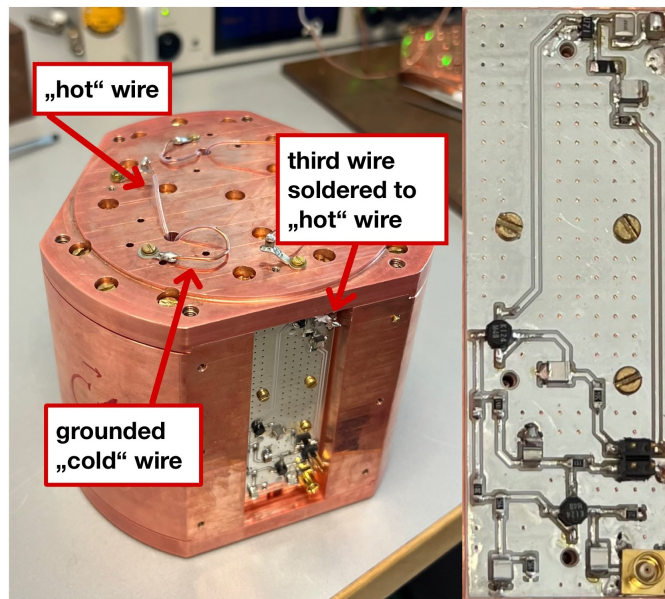

Figure 19: Experimental setup of the signal measurement with a cryogenic amplifier. Left: Implementation of the amplifier into the detection setup; the printed circuit board of the amplifier is screwed onto the side of the Cu-housing. The third wire, soldered to the "hot" wire end of the coil is capacitively coupled to the amplifier circuit. Right: Close-up of the new amplifier circuit board.

Two more coils with the same design as the one described above were made and used to test three new amplifiers simultaneously. The results are listed in

table 10. To keep the suppression of the Q-factor as minimal as possible a small

Table 10: Q-factor of the resonance signal detected with the new amplifier.

$\nu_{0,20\,pF+amp}$ at $300\,\mathrm{K}$	Q-factor at $300\,\mathrm{K}$	$\nu_{0,20\,pF+amp}$ at $4\,\mathrm{K}$	Q-factor at $4\,\mathrm{K}$
$34.45\,\mathrm{MHz}$	400	$34.13\,\mathrm{MHz}$	1200
$34.15\,\mathrm{MHz}$	240	$33.97\,\mathrm{MHz}$	340
$36.60\,\mathrm{MHz}$	350	$36.31\,\mathrm{MHz}$	450

coupling capacitance of $1.95\,\mathrm{pF}$ was used. The performance of the three new amplifiers is very different. There seems to be a problem with the second and third amplifier, both performed much worse than the first one, where a maximum Q-factor of 1200 was reached. The obtained frequency spectra are shown in figure 20, 21 and 22. Each resonance signal is at least $16\,\mathrm{dBm}$ higher than the underlaying noise signal. Additionally one can clearly see some equidistant noise peaks spread out over the spectrum. When the amplifier was turned down, so were the peaks. It is not exactly clear, where they come from, the coldhead pump was momentarily turned off for the duration of the measurements.
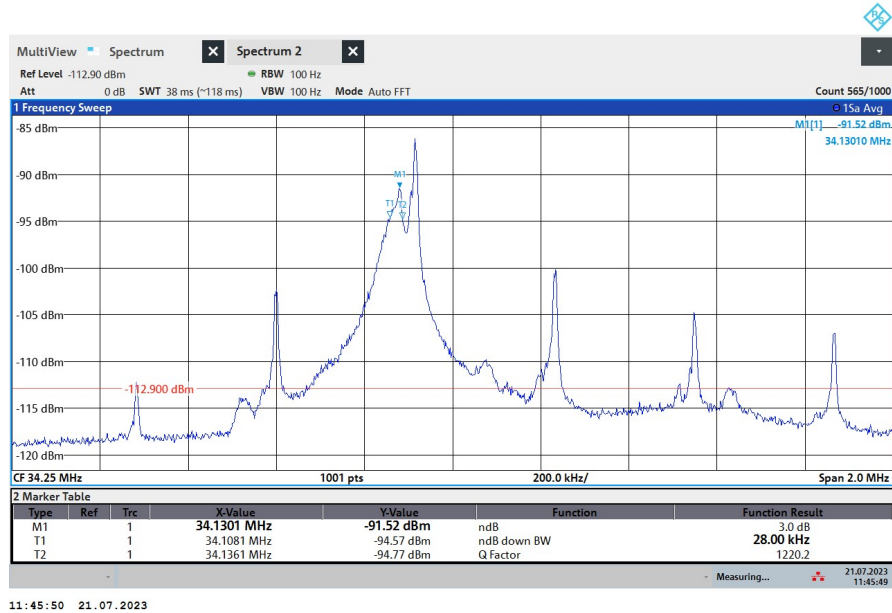

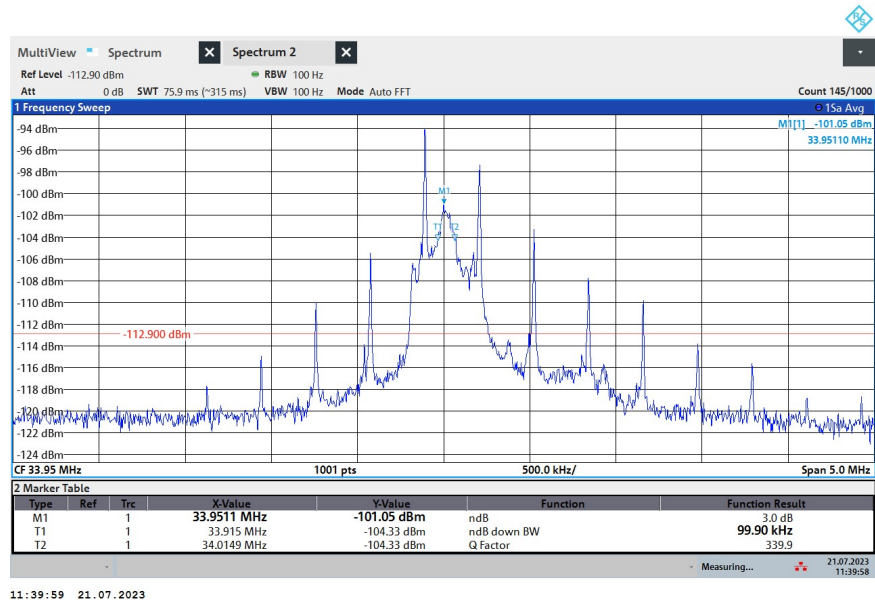**Figure 20:** Frequency spectrum of the signal detected by the new amplifiers no.1.

Figure 21: Frequency spectrum of the signal detected by the new amplifiers no.2.
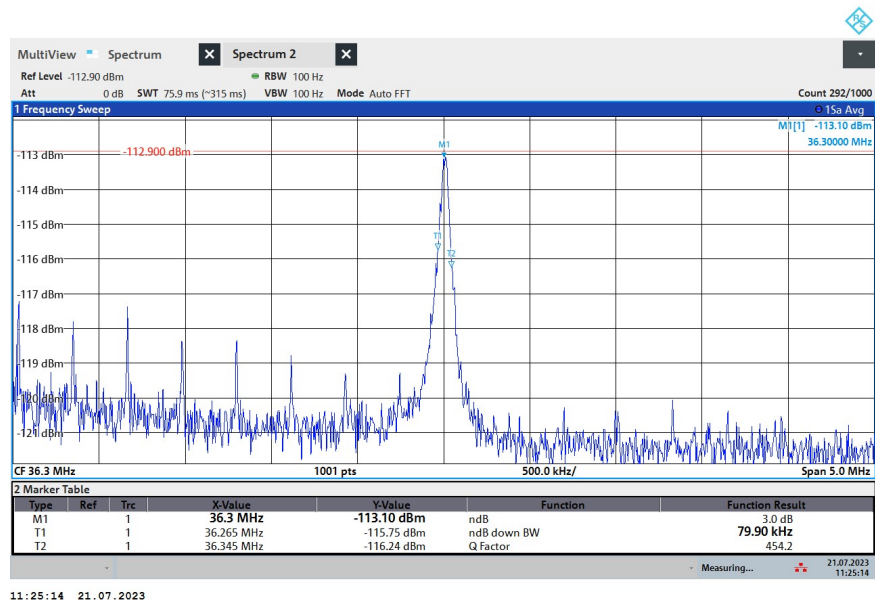

Figure 22: Frequency spectrum of the signal detected by the new amplifiers no.3.

Using the measurements of the resonance frequencies and the previously calculated self-capacitances of the coils, it is also possible to calculate the self-capacitance of the amplifier. A simplified depicition of the total circuit can be seen in figure 23.
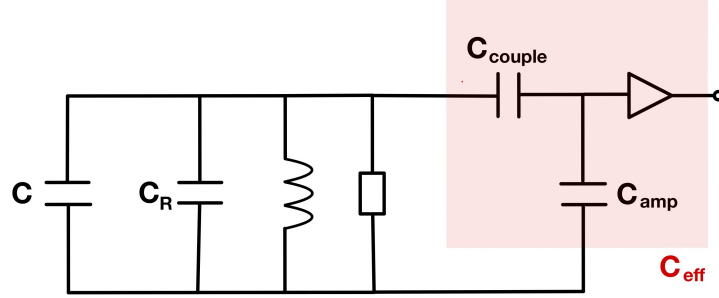

Figure 23: Simplified depiction of the total circuit. A capacitance $C=20\,\mathrm{pF}$ is used to simulate the trap capacitance. The coupling capacitance C_{couple} is $1.95\,\mathrm{pF}$. The self-capacitance of the resonant circuit C_R and the self-capacitance of the amplifier C_{amp} are experimentally determined.

The total capacitance of the circuit is given by

$$C_{total} = C + C_R + C_{eff}. \tag{27}$$

Using equation (24) with the additional capacitance $C_{additional} = C + C_{eff}$ the effective capacitance C_{eff} of the amplifier can be calculated with

$$C_{eff} = C_R \cdot \left(\left(\frac{\nu_{0,free}}{\nu_{0,C_{additional}}} \right)^2 - 1 \right) - C. \tag{28}$$

C_{eff} consists of the coupling capacitance C_{couple} and the self-capacitance of the amplifier C_{amp} connected in series. Therefore the self-capacitance of the amplifier can be calculated with

$$\frac{1}{C_{amp}} = \frac{1}{C_{eff}} - \frac{1}{C_{couple}}. \tag{29}$$

The results are listed in table 11.

Table 11: Self-capacitance of the amplifier. The self-capacitance of the resonant circuit was calculated and then used to determine C_{amp}. The listed resonance frequencies were measured at room temperature.

$\nu_{0,free}$	$\nu_{0,20\,pF}$	C_R	$\nu_{0,20\,pF+amp}$	C_{eff}	C_{amp}
68.70 MHz	35.40 MHz	7.23 pF	34.15 MHz	1.52 pF	0.85 pF
63.30 MHz	34.90 MHz	8.73 pF	34.45 MHz	1.26 pF	0.77 pF
71.55 Mhz	37.60 MHz	7.63 pF	36.60 MHz	1.53 pF	0.86 pF

7 Results and Outlook

Over the course of this bachelor thesis toroidal cyclotron resonators were designed and characterised for the future measurement of the mass of ^{133}Cs at the PENTATRAP experiment. After a brief summary of the theory behind Penning traps and how the eigenmotions of a trapped ion are measured, the design process of the resonant circuit was discussed.

A Q-factor of the free resonant circuit of >1600 was repeatedly reached using coils made with Cu-wire. The results were consistent and reproducible. A maximal Q-factor of 4240 was reached with a coil made from superconducting NbTi-wire. However, the Q-factors of NbTi-coils showed large fluctuations, the main problem seemed to be a bad thermal connection to the short Cu-wire ends. An improvement of the Q-factor about 600 was made, when Sn96.5Ag3Cu0.5-solder was used instead of regular Sn60Pb38Cu2-solder. When the wires were welded together, the Q-factor improved about 440.

In the next part, the resonance frequency was tuned using varactor diodes. A maximal tuning range of 3.95 Mhz was achieved with three varactor diodes, which corresponds to about 11% of the targeted resonance frequency. Simultaneously, the Q-factor decreased about up to 20%. With the resonant circuit using the Cu-coils made with the new design, this would still result in Q-factors of >1300.

In the last part, the resonance signal of the Cu-resonator was detected with an cryogenic amplifier. With the new amplifier design and a weak coupling resistance of 1.95 pF, a maximal Q-factor of 1200 was measured.

The next step would be to detect the resonator signal with the amplifier and simultaneously use varactor diodes to tune the resonance frequency. Since a Q-factor of 1200 was measured and the varactor circuit causes a decrease of the Q-factor of up to 20%, a Q-factor of just below 1000 can be expected. Apart from determining the Q-factor of the resonant circuit, there were also no further measurements with NbTi-coils conducted. Since the Q-factor is expected to decrease in the magnetic field due to the flux-flow-resistance, measurements on the extend of this decrease should be done in the 7 T field of the PENTATRAP magnet during the next upgrade of the PENTATRAP setup.

References

1. Parker, R., Yu, C., Zhong, W., Estey, B. & Müller, H. Measurement of the Fine Structure Constant as a Test of the Standard Model. *Science* **360,** 191–195 (2018).

2. *An atomic fountain for measuring the fine-structure constant* http://matterwave.physics.berkeley.edu/cesium-fountain. [Online; accessed 28-July-2023].

3. Paul, W. Electromagnetic traps for charged and neutral particles. *Rev. Mod. Phys.* **62,** 531–540 (1990).

4. Van Dyck, R., Schwinberg, P. & Dehmehlt, H. Electron magnetic moment from geonium spectra: Early experiments and background concepts. *Phys. Rev. D* **34,** 722 (1986).

5. Sturm, S. *et al.* The ALPHATRAP experiment. *Eur. Phys. J. Special Topics* **227,** 1425–1491 (2019).

6. Repp, J. *et al.* PENTATRAP: a novel cryogenic multi-Penning-trap experiment for high-precision mass measurements on highly charged ions. *Appl. Phys. B* **107(4),** 983–996 (2012).

7. Weigel, A. *Aufbau und Charakterisierung von Axialfrequenzverstärkern für das PENTATRAP-Experiment.* Bachelor thesis (University of Heidelberg, 2011).

8. Earnshaw, S. On the Nature of the Molecular Forces which Regulate the Constitution of the Luminiferous Ether. *Trans. Cambridge Philos.* **7(1),** 97–112 (1842).

9. Gabrielse, G., Haarsma, L. & Rolston, S. Open-endcap Penning traps for high precision experiments. *Int. J. Mass Spectrom. Ion Proc.* **88,** 319–332 (1989).

10. Vogel, M. *Particle Confinement in Penning Traps. An Introduction* 22–29 (Springer, 2018).

11. Tan, J. & Gabrielse, G. One electron in an orthogonalized cylindrical Penning trap. *Appl. Phys. Lett.* **55,** 2144–2146 (1989).

12. Kromer, K. *et al.* High-precision mass measurement of doubly magic ^{208}Pb. *Eur. Phys. J. A* **7,** 202 (2022).

13. Rischka, A. *et al.* Mass-Difference Measurements on Heavy Nuclides with an eV/c^2 Accuracy in the PENTATRAP Spectrometer. *Phys. Rev. Lett.* **124(11),** 113001 (2020).

14. Mooser, A. *et al.* Towards a direct measurement of the g-factor of a single isolated proton. *Can. J. Phys.* **89,** 165–168 (2011).

15. Brown, L. & Gabrielse, G. Geonium Theory: Physics of a single electron or ion in a Penning trap. *Rev. Mod. Phys.* **58(1),** 233–311 (1986).

16. Gabrielse, G. Why Is Sideband Mass Spectrometry Possible with Ions in a Penning Trap? *Phys. Rev. Lett.* **102(17),** 172501 (2009).

17. Gabrielse, G. The true cyclotron frequency for particles and ions in a Penning trap. *Int. J. Mass Spectrom.* **279,** 107–112 (2009).

18. Major, F., Gheorghe, V. & Werth, G. *Charged Particle Traps: Physics and Techniques of Charged Particle Field Confinement* (Springer, 2005).

19. Dilling, J., Blaum, K., Brodeur, M. & Eliseev, S. Penning-Trap Mass Measurements in Atomic and Nuclear Physics. *Annu. Rev. Nucl. Part. Sci.* **68,** 45–74 (2018).

20. Dehmelt, H. & Walls, F. 'Bolometric' Technique for the rf Spectroscopy of Stored Ions. *Phys. Rev. Lett.* **21,** 127–131 (1968).

21. Wineland, D. & Dehmelt, H. Principles of the stored ion calorimeter. *J. Appl. Phys.* **46,** 919–930 (1975).

22. Church, D. & Dehmelt, H. Radiative Cooling of Electrodynamically Contained Proton Gas. *J. Appl. Phys.* **40(9),** 3421–3424 (1969).

23. Cornell, E. *et al.* Mode coupling in a Penning Trap: π pulses and a classical avoided crossing. *Phys. Rev. A* **41 (1),** 312–315 (1990).

24. Verdú, J. *et al.* Determination of the g-Factor of Single Hydrogen-Like Ions by Mode Coupling in a Penning Trap. *Phys. Scr.* **T112,** 68–72 (2004).

25. Horowitz, P. & Hill, W. *The Art of Electronics* (Cambridge University Press, 1989).

26. Hickman, I. *Analog Electronics: Analog Circuitry Explained* 42 (Heinemann Newnes, 2013).

27. Johnson, J. Thermal Agitation of Electricity in Conductors. *Phys. Rev.* **32,** 97–109 (1928).

28. Nyquist, H. Thermal Agitation of Electric Charge in Conductors. *Phys. Rev.* **32,** 110–113 (1928).

29. Itano, W., Bergquist, J., Bollinger, J. & Wineland, D. Cooling methods in ion traps. *Phys. Scr.* **1995(T59),** 106–120 (1995).

30. Egl, A. *High-Precision Laser Spectroscopy of the Fine Structure in* $^{40}\text{Ar}^{13+}$ *at ALPHATRAP.* PhD thesis (University of Heidelberg, 2020).

31. Schüssler, R. *A new Detection System for the high-precision Penning-trap mass spectrometer PENTATRAP.* Master thesis (University of Heidelberg, 2015).

32. Hrmo, P. *et al.* Sideband cooling of the radial modes of motion of a single ion in a Penning trap. *Phys. Rev. A* **100,** 043414 (2019).

33. Dehmelt, H. Entropy reduction by motional sideband excitation. *Nature* **262(5571),** 777 (1976).

34. Van Dyck, R., Ekstrom, P. & Dehmelt, H. Axial, magnetron, cyclotron and spin-cyclotron-beat frequencies measured on single electron almost at rest in free space (geonium). *Nature* **262(5571),** 776–777 (1976).

35. Ketterer, J. *et al.* First-order perturbative calculation of the frequency-shifts caused by static cylindrically-symmetric electric and magnetic imperfections of a Penning trap. *Int. J. Mass Spectrom.* **358,** 1–16 (2014).

36. Ketterer, J. *et al.* Classical calculation of relativistic frequency-shifts in an ideal Penning trap. *Int. J. Mass Spectrom.* **361,** 34–40 (2014).

37. Bollen, G. *et al.* The accuracy of heavy-ion mas measurements using time of flight-ion cyclotron resonance in a penning trap. *J. Appl. Phys.* **68 (9),** 4355–4374 (1990).

38. Müller, M. *Design and implementation of a non-destructive ion detection system for the Heidelberg* ^{3}He *g-factor experiment.* Master thesis (University of Heidelberg, 2020).

39. Wheeler, H. A. Formulas for the Skin Effect. *PIRE* **30(9),** 412–424 (1942).

40. Duthil, P. *Materials properties at low temperature* `https://indico.cern.ch/event/194284/contributions/1472798/attachments/281498/393574/CAS_propmat_2013.pdf`. [Online; accessed 24-July-2023]. 2013.

41. *Thin Metal Foil Thermal Straps - Copper Purity and RRR* `https://thermal-space.com/thermal-straps/thin-metal-foil-thermal-straps/`. [Online; accessed 30-July-2023].

42. Shapira, Y. & Neuringer, L. Upper Critical Fields of Nb-Ti Alloys: Evidence for the Influence of Pauli Paramagnetism. *Phys. Rev.* **140,** A1638–A1644 (1965).

43. Weigel, A. *Entwicklung des kryogenen Nachweissystems für ALPHATRAP und THe-Trap.* Master thesis (University of Heidelberg, 2014).

44. Ulmer, S. *et al.* The quality factor of a superconducting rf resonator in a magnetic field. *Rev. Sci. Instrum* **80,** 123302 (2009).

45. Ulmer, S. *Entwicklung eines experimentellen Aufbaus zur Messung des g-Faktors des Protons in einer Penning-Falle.* Diploma thesis (University of Mainz, 2006).

46. Devlin, J. *et al.* Superconducting Solenoid System with Adjustable Shielding Factor from Precision Measurements of the Porperties of the Antiproton. *Phys. Rev. Applied* **12,** 044012 (2019).

Danksagung

Besonderer Dank geht raus an

Klaus Blaum, für die Möglichkeit, meine Bachelorarbeit am MPIK durchführen zu können und den Einsatz bezüglich der Korrektur dieser Arbeit.

Sergey Eliseev, für die Betreuung meiner Arbeit vor Ort, die Korrektur dieser Arbeit und die Unterstützung bei der Durchführung verschiedenster Messungen.

José Crespo, für die kurzfristige Übernahme der Zweitkorrektur dieser Arbeit.

Menno Door, **Kathrin Kromer** und **Jost Herkenhoff**, für die Unterstützung bei Fragen vor Ort, die Korrektur dieser Arbeit und sämtliche Verbesserungsvorschläge.

meine Freunde aus der Uni, ohne die ich vermutlich nie bis an diesen Punkt in meinem Studium gekommen wäre.

meine WG, für die alltägliche Unterstützung und Ablenkung und für Euer Verständnis und Eure Geduld in stressigen Zeiten.

meine Eltern, die mich seit ich denken kann bei allem, was ich tue, unterstützen und mir das Studium überhaupt erst ermöglicht haben.